

Dear Author

Please use this PDF proof to check the layout of your article. If you would like any changes to be made to the layout, you can leave instructions in the online proofing interface. First, return to the online proofing interface by clicking "Edit" at the top of the page, then insert a Comment in the relevant location. Making your changes directly in the online proofing interface is the quickest, easiest way to correct and submit your proof.

Please note that changes made to the article in the online proofing interface will be added to the article before publication, but are not reflected in this PDF proof.

If you would prefer to submit your corrections by annotating the PDF proof, please download and submit an annotatable PDF proof by clicking the button below.

 [Annotate PDF](#)

We have presented the Graphical Abstract text and image for your article below. This brief summary of your work will appear in the contents pages of the issue in which your article appears.

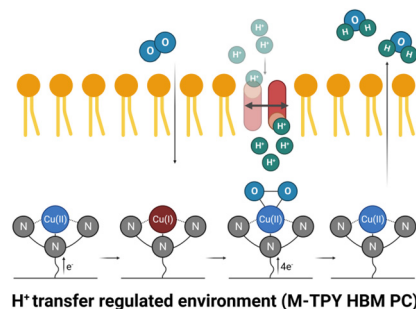
1

Protonic nanoenvironment engineering for tuning the electrocatalytic efficiency and product selectivity of O₂ reduction

Hei Tung Yau, Zuo Hang Yu and Edmund C. M. Tse*

Precise control over the activity and selectivity of oxygen reduction reaction (ORR) catalysts is key to the development of efficient and durable cathodes for proton-exchange membrane (PEM) fuel cells.

Q2



Please check this proof carefully. Our staff will not read it in detail after you have returned it.

Please send your corrections either as a copy of the proof PDF with electronic notes attached or as a list of corrections. **Do not edit the text within the PDF or send a revised manuscript** as we will not be able to apply your corrections. Corrections at this stage should be minor and not involve extensive changes.

Proof corrections must be returned as a single set of corrections, approved by all co-authors. No further corrections can be made after you have submitted your proof corrections as we will publish your article online as soon as possible after they are received.

Please ensure that:

- The spelling and format of all author names and affiliations are checked carefully. You can check how we have identified the authors' first and last names in the researcher information table on the next page. **Names will be indexed and cited as shown on the proof, so these must be correct.**
- Any funding bodies have been acknowledged appropriately and included both in the paper and in the funder information table on the next page.
- All of the editor's queries are answered.
- Any necessary attachments, such as updated images or ESI files, are provided.

Translation errors can occur during conversion to typesetting systems so you need to read the whole proof. In particular please check tables, equations, numerical data, figures and graphics, and references carefully.

Please return your **final** corrections, where possible within **48 hours** of receipt, by e-mail to: InorgChemFrontiersPROD@rsc.org. If you require more time, please notify us by email.

Funding information

Providing accurate funding information will enable us to help you comply with your funders' reporting mandates. Clear acknowledgement of funder support is an important consideration in funding evaluation and can increase your chances of securing funding in the future.

We work closely with Crossref to make your research discoverable through the Funding Data search tool (<http://search.crossref.org/funding>). Funding Data provides a reliable way to track the impact of the work that funders support. Accurate funder information will also help us (i) identify articles that are mandated to be deposited in **PubMed Central (PMC)** and deposit these on your behalf, and (ii) identify articles funded as part of the **CHORUS** initiative and display the Accepted Manuscript on our web site after an embargo period of 12 months.

Further information can be found on our webpage (<http://rsc.li/funding-info>).

What we do with funding information

We have combined the information you gave us on submission with the information in your acknowledgements. This will help ensure the funding information is as complete as possible and matches funders listed in the Crossref Funder Registry.

If a funding organisation you included in your acknowledgements or on submission of your article is not currently listed in the registry it will not appear in the table on this page. We can only deposit data if funders are already listed in the Crossref Funder Registry, but we will pass all funding information on to Crossref so that additional funders can be included in future.

Please check your funding information

The table below contains the information we will share with Crossref so that your article can be found *via* the Funding Data search tool. **Please check that the funder names and grant numbers in the table are correct and indicate if any changes are necessary to the Acknowledgements text.**

Funder name	Funder's main country of origin	Funder ID (for RSC use only)	Award/grant number
National Natural Science Foundation of China	China	501100001809	22002132
Science, Technology and Innovation Commission of Shenzhen Municipality	China	501100010877	JCYJ20210324122011031
Research Grants Council, University Grants Committee	Hong Kong	501100002920	17308323 207301212 207301251 27301120 E-HKU704/19 T23-713/22-R

Researcher information

Please check that the researcher information in the table below is correct, including the spelling and formatting of all author names, and that the authors' first, middle and last names have been correctly identified. **Names will be indexed and cited as shown on the proof, so these must be correct.**

If any authors have ORCID or ResearcherID details that are not listed below, please provide these with your proof corrections. Please ensure that the ORCID and ResearcherID details listed below have been assigned to the correct author. Authors should have their own unique ORCID iD and should not use another researcher's, as errors will delay publication.

Please also update your account on our online [manuscript submission system](#) to add your ORCID details, which will then be automatically included in all future submissions. See [here](#) for step-by-step instructions and more information on author identifiers.

First (given) and middle name(s)	Last (family) name(s)	ResearcherID	ORCID iD
Hei Tung	Yau		
Zuo Hang	Yu		
Edmund C. M.	Tse	E-5309-2019	0000-0002-9313-1290

Queries for the attention of the authors

Journal: **Inorganic Chemistry Frontiers** Paper: **d3qi01756g**

Title: **Protonic nanoenvironment engineering for tuning the electrocatalytic efficiency and product selectivity of O₂ reduction**

For your information: You can cite this article before you receive notification of the page numbers by using the following format: (authors), Inorg. Chem. Front., (year), DOI: 10.1039/d3qi01756g.

Editor's queries are marked like this **Q1**, **Q2**, and for your convenience line numbers are indicated like this 5, 10, 15, ...


Please ensure that all queries are answered when returning your proof corrections so that publication of your article is not delayed.

Query Reference	Query	Remarks
Q1	Have all of the author names been spelled and formatted correctly? Names will be indexed and cited as shown on the proof, so these must be correct. No late corrections can be made.	
Q2	Please check that the inserted Graphical Abstract text is suitable. If you provide replacement text, please ensure that it is no longer than 250 characters (including spaces).	
Q3	The sentence beginning "Finally, to the filtered solution ..." has been altered for clarity. Please check that the meaning is correct.	
Q4	Have all of the funders of your work been fully and accurately acknowledged? If not, please ensure you make appropriate changes to the Acknowledgements text.	
Q5	Ref. 6: Please provide the page (or article) number(s).	

RESEARCH ARTICLE

Protonic nanoenvironment engineering for tuning the electrocatalytic efficiency and product selectivity of O₂ reduction†

Cite this: DOI: 10.1039/d3qi01756g

Hei Tung Yau, Zuo Hang Yu and Edmund C. M. Tse *

Precise control over the activity and selectivity of oxygen reduction reaction (ORR) catalysts is key to the development of efficient and durable cathodes for proton-exchange membrane (PEM) fuel cells. Recently, hybrid bilayer membranes (HBMs) have emerged as nanoscale electrochemical platforms for investigating proton-coupled electron transfer (PCET) reactions, with particular emphasis on ORR thermodynamics and kinetics. In this work, we have developed a unique HBM incorporating a new self-assembled monolayer (SAM) design, deviating from the established nanoconstructs in prior studies. The new design integrates a custom-synthesized tridentate ligand, 2,2':6',2''-terpyridine-4'-oxy-hexane-1-thiol (TPY), for hosting first-row transition metals (M) beyond Cu(II), including Ni(II) and Mn(II), resulting in a SAM decorated with terminal mononuclear M-TPY complexes. Among the observed ORR activity and selectivity, Cu-TPY SAM showed distinctive characteristics in contrast to Ni-TPY SAM and Mn-TPY SAM. Cu-TPY SAM exhibited significantly higher ORR activity via a dissociative 4-electron ORR mechanism, while Ni-TPY SAM and Mn-TPY SAM displayed lower ORR activity employing an associative 2-electron ORR pathway. We attributed these differences to the formation of distinct M–O intermediates, specifically end-on metal-superoxo adducts ($\eta^1 \text{M}-\text{O}_2^-$) and side-on metal-superoxo adducts ($\eta^2 \text{M}-\text{O}_2^-$), upon O₂ binding to the metal center. By appending a 1,2-dimyristoyl-*sn*-glycero-3-phosphocholine (DMPC) lipid monolayer onto M-TPY SAM to form M-TPY HBM, the catalyst–nanoenvironment interface transitions from one with facile proton transfer to one with protons depleted. With the incorporation of dodecyl boronic acid (DBA) as a proton carrier (PC) into the lipid monolayer to form M-TPY HBM DBA, the nanoenvironment switches to one with regulated proton transfer kinetics, ultimately achieving systematic modulation of the ORR activity and selectivity of the embedded M-TPY catalytic site. The mechanistic insights gained on steering the PCET pathways have implications for boosting the activity and selectivity of electrocatalysts tailored for facilitating other redox reactions central to renewable energy schemes and sustainable resource utilization.

Received 31st August 2023,
Accepted 27th October 2023

DOI: 10.1039/d3qi01756g

rsc.li/frontiers-inorganic

1. Introduction

The increasing global energy demand and the urgent need to address excessive emissions of greenhouse gases and air pollutants have led to extensive research on renewable power sources.^{1,2} Among these alternatives, hydrogen fuel cells have emerged as a promising solution for generating electricity with zero emission.^{3–10} In a proton-exchange membrane (PEM) fuel cell, one of the promising hydrogen fuel cells, electricity is produced

through the electrochemical conversion of hydrogen and oxygen gases. This conversion process involves two separate reactions: the hydrogen oxidation reaction (HOR) taking place at the anode and the oxygen reduction reaction (ORR) occurring at the cathode.^{11–16}

The ORR, which involves proton-coupled electron transfer (PCET), is a crucial half-cell reaction in PEM fuel cells.^{17–20} However, the main challenge for commercializing PEM fuel cells is the slow kinetics of the ORR. The sluggish kinetics of the ORR can be attributed to several factors. One primary reason is the high energy activation barriers associated with interfacial O₂ adsorption, O=O bond breaking, and H₂O product removal from the electrode.^{21–27} Another factor is the mismatch between the rates of proton and electron transfer.^{28,29} Combining both factors leads to the formation of multiple pathways for the ORR, ultimately resulting in deceleration of the reaction kinetics.

Department of Chemistry, HKU-CAS Joint Laboratory on New Materials, University of Hong Kong, Hong Kong SAR, China. E-mail: ecmtse@hku.hk

† Electronic supplementary information (ESI) available: SAM synthesis, HBM fabrication, experimental details, Fig. S1–S11, Table S1, and additional data including NMR, ICP-MS, CV, and LSV as discussed in the main text. See DOI: <https://doi.org/10.1039/d3qi01756g>

Generally, there are four ORR mechanisms: 1-electron, associative 2-electron, associative 4-electron, and dissociative 4-electron transfer pathways (Fig. 1).^{30,31} The 1-electron transfer pathway occurs when the rate of proton transfer to the active sites of the ORR is significantly slower than that of electron transfer, resulting in a facile 1-electron reduction of O_2 into superoxide. The associative 2-electron transfer pathway and the dissociative 4-electron transfer pathway occur when the protons and electrons are transferred to the ORR active sites simultaneously. However, in the associative 2-electron transfer pathway, the rate of O–O bond breaking is slower than that of protonation of O_2 , while in the dissociative 4-electron transfer pathway, the O–O bond breaking precedes the protonation of O_2 . The 1-electron and associative 2-electron transfer pathways are undesirable in PEM fuel cell operation because they generate superoxide anions (O_2^-) and hydrogen peroxide (H_2O_2), respectively, which are detrimental to the device components. The most desirable ORR mechanism is the dissociative 4-electron transfer pathway, as it maximizes chemical-to-electrical energy conversion and exclusively produces water as the only product.

Despite the development of the highly efficient 20 wt% Pt/C catalyst (platinum nanoparticles supported on carbon black) for the ORR, it remains necessary to incorporate a relatively high platinum loading ($\sim 0.4 \text{ mg cm}^{-2}$) in the catalyst layers of fuel cell systems.^{32–35} This substantial platinum requirement accounts for a significant portion of the total cost. Furthermore, Pt-based electrocatalysts are prone to degradation over time, primarily as a result of surface oxidation, dissolution, and aggregation, particularly in alkaline environments.³⁶ To enhance the kinetics of the ORR and mitigate the cost associated with electrocatalysts, two common approaches are frequently employed. The first approach involves the design of non-precious metal electrocatalysts that exhibit performance comparable to that of their precious metal counterparts.^{37–45} However, due to the inherent properties of metal centers, most non-precious metal electrocatalysts predominantly promote either a 2-electron ORR pathway or a mixture of 2-electron and 4-electron ORR mechanisms, leading to the formation of either H_2O_2 as the major product or a

mixture of H_2O_2 and water. This compromises the lifetime and efficiency of electrocatalytic devices. The second approach entails delving into the fundamental aspects of ORR kinetics, with a particular emphasis on the rates of proton and electron transfer.^{28,29,46–48} Our research group adopted the second approach, which involves modifying the protonic nanoenvironments of ORR electrocatalysts through the use of a nanoscale electrochemical platform known as a hybrid bilayer membrane. Through this approach, we aimed to conduct an insightful investigation into the proton transfer kinetics and its subsequent impacts on the ORR kinetics and mechanism.

A hybrid bilayer membrane (HBM) is an electrochemical platform designed to investigate the thermodynamics and kinetics of PCET processes, with a specific focus on the kinetics of the ORR.^{28,29,46–51} With its unique structural features, a HBM enables the study of proton transfer kinetics and its subsequent impacts on the ORR kinetics and mechanism. A HBM consists of a layered structure, beginning with a self-assembled monolayer (SAM) of ORR electrocatalysts anchored onto a gold (Au) electrode (Fig. 2). This SAM serves as an electrocatalytically active site for the ORR, facilitating the necessary electrochemical process. On top of the SAM, a monolayer of lipids is appended through van der Waals forces. This lipid monolayer serves as a physical barrier to minimize proton transfer kinetics. Apart from contributing to the overall structure of the HBM, the lipid membrane can be embedded with a proton carrier (PC), allowing for the recovery and regulation of transmembrane proton transfer kinetics. Controlling the rate of proton transfer to the SAM of ORR electrocatalysts can consequently influence the kinetics and mechanism of the ORR.

Previous studies on HBM-based ORR electrocatalysis have primarily focused on a specific system known as Cu-BTT HBM (Cu-BTT = binuclear copper complex of 6-((3-(benzylamino)-1,2,4-triazol-5-yl)amino)hexane-1-thiol).^{28,29,47,48,50,51} The investigations of Cu-BTT HBM have demonstrated its remarkable characteristics, including a significant current enhancement in oxygen reduction electrocatalysis and a highly selective 4-electron ORR mechanism when 10 mol% dodecyl boronic acid (DBA) proton carriers were incorporated into the lipid membrane. However, it is important to note that the for-

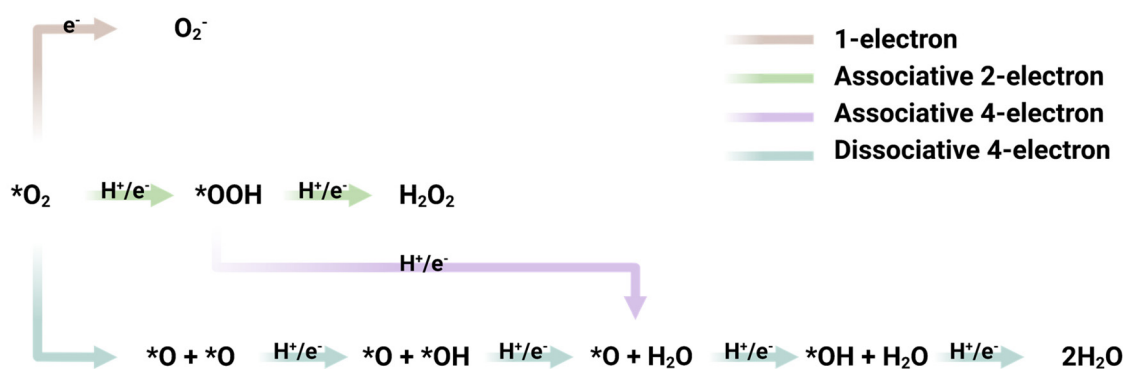


Fig. 1 Multiple ORR mechanisms arise from two key factors: (1) high energy activation barriers associated with oxygen bond breaking and (2) a mismatch between rates of proton and electron transfer, leading to deceleration of reaction kinetics (ORR = oxygen reduction reaction).

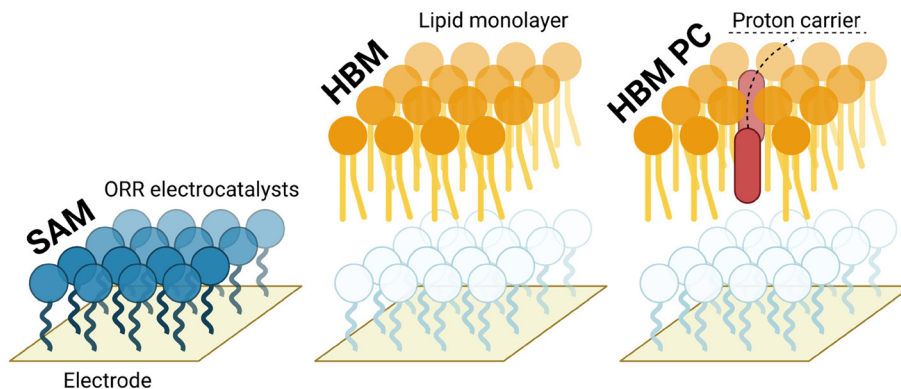


Fig. 2 Layered structure of a HBM with the bottom layer comprising a SAM of ORR electrocatalysts anchored onto an Au electrode, followed by the top layer comprising a lipid monolayer, without and with a PC, held in place by van der Waals forces (SAM = self-assembled monolayer; HBM = hybrid bilayer membrane; PC = proton carrier).

mation of Cu-BTT SAM is highly sensitive to the metal–ligand ratio and the ligand surface density. This ligand surface density is due to the need for two triazole-based ligands attached onto the substrate in close proximity for efficient coordination with two Cu(II) ions in a paired configuration.

In this work, we have developed a new HBM with a tailored SAM design which differs from previous studies that used Cu-BTT SAM and effectively resolves concerns regarding the metal–ligand ratio and the ligand surface density. This new design incorporates a mononuclear first-row transition metal complex with a specific tridentate ligand, denoted as M-TPY SAM, where M represents first-row transition metals and TPY stands for 2,2':6',2''-terpyridine-4'-oxy-hexane-1-thiol. In addition to Cu(II), we expanded our investigation to include other first-row transition metals, such as Ni(II) and Mn(II), which have been previously reported to exhibit ORR activity.^{52–55} To address concerns about the metal–ligand ratio and the ligand surface density, we specifically selected the TPY ligand because of its ability to form single-site one-to-one metal–ligand coordination independently. Moreover, the TPY ligand features a stable tridentate mononuclear complex with a metal ion, providing improved stability compared to dinuclear Cu-BTT due to stronger metal coordination. Furthermore, to maintain consistency with previous research, we introduced 1,2-dimyristoyl-*sn*-glycero-3-phosphocholine (DMPC) as the lipid source and doped DBA proton carriers within the DMPC lipid monolayer. This configuration allows for the regulation of transmembrane proton delivery, modulating the kinetics and mechanism of the ORR process.

2. Experimental section

2.1. Materials and methods

Chemicals were purchased from commercial sources and used without further purification unless explicitly stated otherwise. For experiments conducted at pH 7, sodium phosphate buffer solutions (100 mM) were prepared using Milli-Q water (>18

MΩ cm⁻¹) and adjusted to the desired pH using H₃PO₄ (85 wt% ACS reagent grade, Sigma-Aldrich) and NaOH (analytical grade, Dieckmann Chemical). Solutions were subjected to a 30 min sparging with N₂ (99.995% high purity grade, Linde HKO) or O₂ (99.995% high purity grade, Linde HKO) prior to each experiment.

2.2. Electrochemical measurements

Electrochemical studies were carried out using a 660E electrochemical workstation (CH Instruments). For studies in aqueous solutions, a three-electrode cell was used with a Pt wire counter electrode and a no-leak Ag/AgCl (3 M KCl) reference electrode. All reported potentials were converted to the RHE scale using the following equation: $E \text{ vs. RHE} = E \text{ vs. Ag/AgCl} + (0.1976 \text{ V}) + ((0.0592 \text{ V}) \times \text{pH})$. The preparation of Au working electrodes followed the same procedure as previously reported.^{28,29,47} A titanium (Ti) adhesion layer (20 nm) beneath an Au layer (100 nm) was deposited on microscope glasses (10 mm width × 10 mm length × 1 mm thickness) using an electron-beam vacuum evaporator (Kao Duen Tech. Corp.). The Au working electrodes were rinsed with water and ethanol prior to use. The formation of a complete lipid layer in the HBM was investigated using an electrochemical blocking assay.^{28,29,47} This blocking assay involved examining the redox behaviour of a solution of K₃Fe(CN)₆ in KCl (1 mM, 100 mM). All experiments were conducted at room temperature (25 ± 1) °C and at least in triplicate. The error bars presented correspond to standard deviations of all trials. Linear sweep voltammetry (LSV) under N₂ and O₂ was carried out at a scan rate of 10 mV s⁻¹. Cyclic voltammetry (CV) for blocking assay was performed at a scan rate of 50 mV s⁻¹.

2.3. Dye-based spectroelectrochemical measurements

A working solution for the colorimetric assay was prepared by adding a solution of Amplex Red (10 mM, 40 μL) in dimethyl sulfoxide (DMSO) in a pH 7 sodium phosphate buffer solution (50 mM, 3.88 mL) that contained horseradish peroxidase (HRP) (10 U mL⁻¹, 80 μL). The working solution (300 μL) was

added to a pH 7 sodium phosphate buffer solution (100 mM, 300 μ L) as an electrolyte before LSV was performed. After the voltammetry was completed, the electrolytic solution was stirred to ensure the homogeneous distribution of H_2O_2 generated during the ORR before measurements. The reaction between Amplex Red and H_2O_2 in the presence of HRP enzyme generates resorufin with an ultraviolet-visible (UV-vis) absorption band (λ_{ex}) at 571 nm (Fig. S1[†]). The intensity of the UV-vis absorbance is dependent on the concentration of H_2O_2 . The amount of H_2O_2 was quantified by placing the electrolytic solution (60 μ L) in a UV-transparent plastic cuvette (Eppendorf, UVette, 10 mm) and subsequently scanning from 300 to 800 nm using a UV-vis spectrophotometer (IMPLEN NanoPhotometer N60). The absorbance of the electrolytic solution was recorded at $\lambda_{\text{ex}} = 571$ nm and subsequently used to calculate the concentration of H_2O_2 , according to the standard curve for H_2O_2 (Fig. S2[†]).

2.4. Calculation methods

The concentration of H_2O_2 generated in the ORR was calculated from the Beer-Lambert law. The sum of electrons involved in the ORR was determined by integrating the corresponding LSV curve to calculate the total charge required for both H_2O_2 and water generation. The calculation methodology is detailed with reference to the previous study (Note S1[†]).²⁹

2.5. HBM fabrication

The preparation of M-TPY HBM followed a similar procedure to that previously described for Cu-BTT HBM, which generally involves three steps: (1) formation of TPY SAM, (2) metal coordination of TPY SAM, and (3) formation of a lipid monolayer on M-TPY SAM to generate M-TPY HBM (Fig. 3). First, TPY was deposited on an Au working electrode *via* the self-assembly process by immersing the electrode in an ethanolic solution of TPY and C5-SH (0.25 mM:12.5 mM, 1:50). The electrode was left in the solution for 2 h and subsequently

rinsed with anhydrous EtOH. Next, metal ions were coordinated onto the TPY-modified Au surface by immersing it in an ethanolic solution of $\text{M}(\text{ClO}_4)_2$ (6.7 mM) for 12 h, where M represents Cu(II), Ni(II), and Mn(II). Metal perchlorate salts were chosen because perchlorates do not undergo redox reactions within the potential window used in this study, and perchlorates are weakly coordinating anions that allow O_2 to engage metal centers readily during the ORR. The electrode was rinsed with anhydrous EtOH and subsequently with a pH 7 sodium phosphate buffer solution (100 mM). Finally, the M-TPY SAM surface was embedded in a monolayer of DMPC lipids by immersing it for 2 h in a pH 7 sodium phosphate buffer solution (100 mM) containing DMPC lipids (0.7 mM) and 1 molar equivalent of DBA proton carriers.

Caution! Perchlorate salts used in HBM fabrication are potentially explosive, toxic, and corrosive. Only small amounts of materials should be prepared.

2.6. TPY preparation

The synthesis of TPY involved three steps: (1) synthesis of *S*-tritylated TPY, (2) deprotection of *S*-tritylated TPY, and (3) dilution of deprotected TPY with alkyl thiol. First, *S*-tritylated TPY was synthesized accordingly (Fig. S3 and S4[†]). Then, the *S*-trityl group of TPY was deprotected by treating a solution of *S*-tritylated TPY (25 mM, 35 μ L) in dichloromethane (DCM) with trifluoroacetic acid (100 μ L), generating a yellow solution. The deprotection reaction was carried out until the solution turned colorless, which was achieved by dropwise addition of triethylsilane (10 μ L). Then, the resulting solution was diluted to a final volume of 3.5 mL using Ar-sparged anhydrous EtOH. Finally, the diluted solution was mixed with alkyl thiol in a ratio of 1:*N* (where alkyl thiol = 1-butanethiol or 1-pentanethiol, *N* = 10, 50, or 100). The selection of alkyl thiol chain length and dilution ratio was optimized based on the structural integrity of the lipid monolayer.

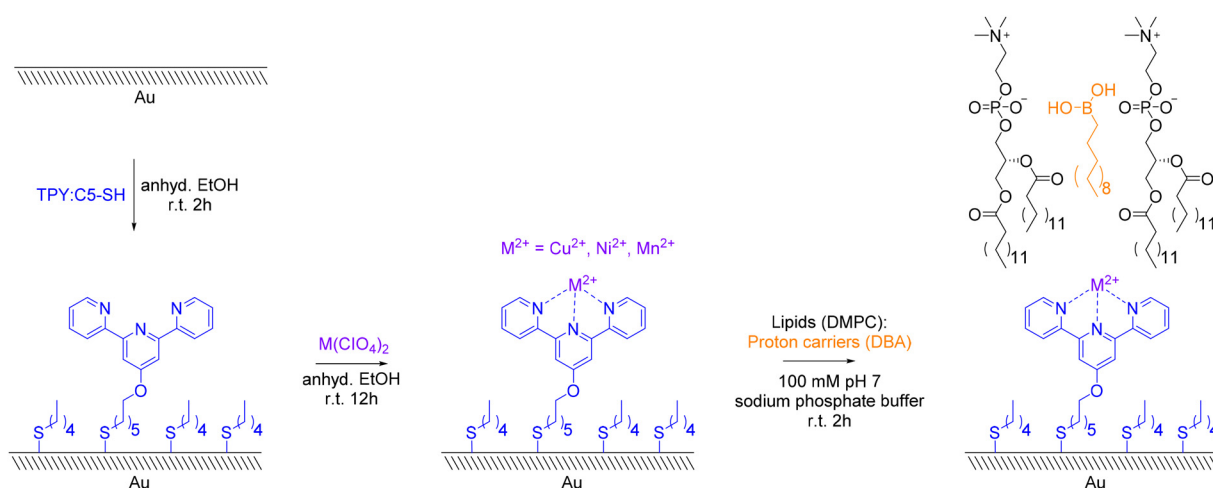


Fig. 3 Schematics illustrating the preparation process of M-TPY SAM, M-TPY HBM, and M-TPY HBM DBA (M = Cu, Ni, Mn).

2.7. Physical characterization

Inductively coupled plasma mass spectrometry (ICP-MS) experiments were performed to quantify the metal content of M-TPY SAM using an ICP mass spectrometer (Agilent 7700x). To prepare the samples for analysis, the Au working electrode containing M-TPY SAM was immersed in a mixed acidic solution of HNO_3 :HCl (1:3, 1 mL) for 12 h. Next, the resulting solution was filtered using a PES syringe filter (Labfil, 0.22 μm). Finally, to the filtered solution (490 μL) was added an internal standard (10 000 ppb Rh, 10 μL) and diluted with 1% HNO_3 (9.5 mL).

^1H NMR and ^{13}C NMR spectroscopy experiments were conducted using a 400 MHz spectrometer (Bruker) to determine the molecular structure of TPY. The sample was dissolved in CDCl_3 and placed in a borosilicate NMR tube (Synthware). NMR spectra were recorded at room temperature (25 ± 1 °C) using 1D ^1H NMR and 1D ^{13}C NMR, respectively. For ^1H NMR, spectral data were acquired with 25 scans and 5 s per scan, while for ^{13}C NMR, 400 scans were employed with 4.5 s per scan. Chemical shifts were calibrated using an internal reference compound, tetramethylsilane (TMS). Subsequent data processing and analysis were performed using MestReNova.

3. Results and discussion

3.1. Optimization of ligand surface density of M-TPY SAM and HBM

Prior to investigating the ORR activity and selectivity of M-TPY SAM and HBM, we initially explored the optimal ligand density of sterically bulky TPY ligands on the Au electrode. The co-presence of TPY ligands and diluent chains is important for creating a tightly packed SAM and subsequently an intact lipid membrane. When TPY ligands assemble on the Au electrode, the terpyridine headgroups create steric repulsion, leading to increased spacing between the ligands. This reduced packing density causes the terpyridine headgroups to

point in random directions, resulting in a disorganized SAM structure. This disordered surface is more likely to have defects such as pinholes, compromising its structural integrity and its ability to block charged and polar species. To examine ORR activity and selectivity while modulating proton transfer kinetics, it is essential to establish the most structurally intact HBM surface. We determined this by measuring the changes in the redox peak potential and current density of the $\text{Fe}(\text{III})/\text{Fe}(\text{II})$ couple before and after M-TPY SAM was embedded within a lipid monolayer. The presence of a positive blocking effect, as manifested through the increased redox peak separation and the decreased current density, implies the constrained diffusion of $\text{Fe}(\text{III})$ ions towards the electrode surface. The most structurally intact HBM surface configuration was achieved by using a SAM of TPY ligands diluted with 1-pentanethiol molecules (C5-SH) in a 1:50 ratio (Fig. 4 and S5[†]). Therefore, we employed M-TPY:C5-SH SAM for preparing HBM platforms and conducting subsequent electrochemical measurements.

3.2. ORR activity of M-TPY SAM

Next, we examined the formation of a TPY SAM on an Au electrode and the subsequent metal coordination by analyzing the changes in the ORR thermodynamics and kinetics, with a specific focus on the shifts in ORR peak potential and current density. During the growth of a SAM of TPY ligands on the Au electrode, we observed a negative shift of 0.065 ± 0.007 V (*versus* RHE) in peak potential and a decrease in current density of 11.7 ± 8.9 $\mu\text{A cm}^{-2}$ (at 0.400 V *versus* RHE) compared to the bare Au electrode (Fig. S6[†]). These results confirm the successful installation of TPY ligands with lower ORR activity onto the Au surface. Furthermore, after metal coordination, we observed a positive shift in peak potential of 0.045 ± 0.012 V (*versus* RHE) and a notable increase in current density of 59.0 ± 15.6 $\mu\text{A cm}^{-2}$ (at 0.400 V *versus* RHE) for Cu-TPY SAM. Similar changes were also observed for Ni and Mn coordination in the TPY SAM. These observations indicate that the

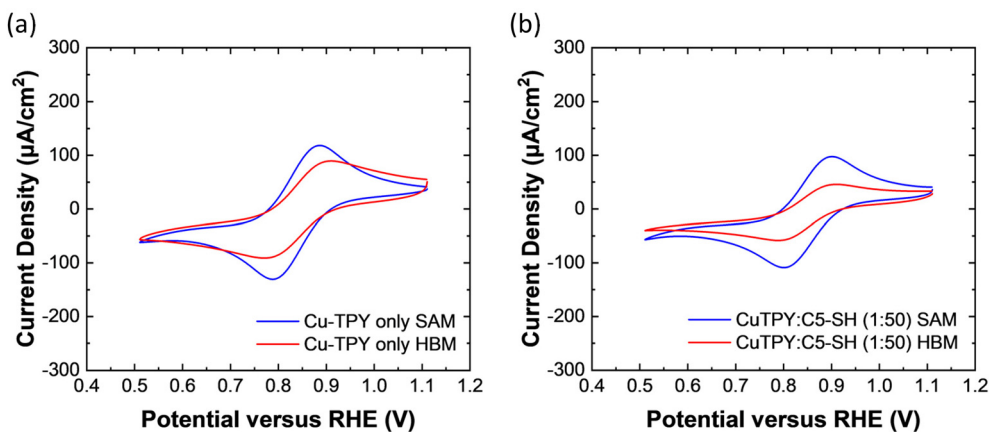


Fig. 4 Effect of ligand dilution ratio on the structural integrity of Cu-TPY HBM. Cyclic voltammograms of a SAM of Cu-TPY, (a) without ligand dilution and (b) diluted with pentanethiol (C5-SH) in a 1:50 ratio (blue), covered by a monolayer of DMPC lipids (red) in a solution of 1 mM $\text{K}_3\text{Fe}(\text{CN})_6$ in 100 mM KCl at a scan rate of 50 mV s^{-1} .

observed ORR activity of M-TPY SAM can be attributed to the coordination of the metal component. Additionally, we confirmed the successful metal coordination by conducting ICP-MS analysis, which measured the corresponding metal content in Cu-TPY SAM, Ni-TPY SAM, and Mn-TPY SAM, respectively (Fig. S7a–c and Table S1†).

During the investigation of the ORR activity of M-TPY SAM, we observed that Cu-TPY SAM exhibited the highest catalytic activity with an ORR current density of $168.4 \pm 18.9 \mu\text{A cm}^{-2}$ at a peak potential of $0.252 \pm 0.012 \text{ V}$ (*versus* RHE) in an O_2 -sparged 100 mM pH 7 sodium phosphate buffer solution. In comparison, Ni-TPY SAM displayed an ORR current density of $57.3 \pm 12.4 \mu\text{A cm}^{-2}$ at a peak potential of $0.282 \pm 0.027 \text{ V}$ (*versus* RHE), whereas Mn-TPY SAM showed an ORR current density of $55.4 \pm 17.5 \mu\text{A cm}^{-2}$ at a peak potential of $0.317 \pm 0.019 \text{ V}$ (*versus* RHE) (Fig. 5a–d). When considering their mass activities with the normalized metal contents (Fig. S7d†), Cu-TPY SAM still demonstrated a higher peak ORR current density of $400.2 \text{ mA cm}^{-2} \text{ mg}_{\text{Cu}}^{-1}$ than both Ni-TPY SAM ($208.0 \text{ mA cm}^{-2} \text{ mg}_{\text{Ni}}^{-1}$) and Mn-TPY SAM ($260.4 \text{ mA cm}^{-2} \text{ mg}_{\text{Mn}}^{-1}$). This phenomenon can be attributed to the nature of the Cu center, including its favourable redox potential and coordination environment for O_2 binding. The initial step of the ORR involves the binding of O_2 to the metal center, necessitating a 1-electron reduction followed by consecutive 1-electron oxidation of the metal center. Theoretically, the favourable redox potential of the Cu(II)/Cu(I) couple ($+0.34 \text{ V}$ *versus* RHE) compared to the Ni(II)/Ni(I) couple (-0.24 V *versus* RHE) and the Mn(III)/(II) couple ($+1.51 \text{ V}$ *versus* RHE) allows Cu(II)/Cu(I) complexes to undergo facile electron transfer with lower energy input, thereby enhancing their reactivity in the ORR. Moreover, considering the varying coordination vacancies of the metal centers, with the tridentate Cu(II) complex having a higher number of coordination vacancies than the tridentate Ni(II) complex and tridentate Mn(III) complex, we suggest that side-on Cu(II)-superoxo ($\eta^2 \text{ Cu-O}_2^-$) intermediates are more likely to be generated during the ORR process.^{56,57} Conversely, end-on Ni(II)-superoxo intermediates ($\eta^1 \text{ Ni-O}_2^-$) and end-on Mn(III)-superoxo intermediates ($\eta^1 \text{ Mn-O}_2^-$) are more likely to be formed.^{58,59} Their distinct O_2 binding modes result in varying O–O bond cleavage kinetics, consequently affecting their ORR kinetics. Additional information concerning O_2 binding modes will be elaborated upon in the forthcoming discussion regarding ORR selectivity.

To ascertain the ORR activity of M-TPY SAM, we conducted an experiment involving a controlled atmosphere of N_2/O_2 gas purging. As expected, a low background current density was observed for Cu-TPY SAM, Ni-TPY SAM, and Mn-TPY SAM in a N_2 -purged 100 mM pH 7 sodium phosphate buffer solution (Fig. S8†). This result indicates that a minimal ORR occurred in the absence of O_2 . Upon purging the solution with O_2 , a significant increase in ORR activity was observed for each M-TPY SAM. This result confirms that the observed ORR current density stems from O_2 . On the other hand, the structural integrity of the lipid monolayer in M-TPY HBM has been verified through positive blocking effects, as evidenced by the substan-

tial separation of redox peaks and decrease in current density of the Fe(III)/Fe(II) couple (Fig. S9†). The presence of an Fe(III)/Fe(II) redox wave suggests no lipid coverage on M-TPY SAM, while the transfiguration or disappearance of the redox wave indicates the formation of an intact DMPC lipid monolayer. The residual redox responses of the Fe(III)/(II) couple could be due to the Fe(III)/(II) ions in the electrolyte diffusing through the minimal defects of the DMPC lipid monolayer within M-TPY HBM and M-TPY HBM DBA and undergoing redox cycling.

3.3. ORR selectivity of M-TPY SAM

Following our investigation of the ORR activity of M-TPY SAMs, we next explored their ORR selectivity by analyzing the variations in the number of electrons transferred per O_2 . During the ORR, Cu-TPY SAM demonstrated a nearly 4-electron transfer pathway ($n = 3.5 \pm 0.3$), whereas both Ni-TPY SAM and Mn-TPY SAM followed a nearly 2-electron transfer pathway ($n = 2.4 \pm 0.4$ and 2.4 ± 0.2), respectively (Fig. 5e). The variations in ORR selectivity between Cu-TPY SAM and the other two can be attributed to the disparities in O_2 binding modes. Generally, there are two potential types of 1:1 M–O adducts with 1-electron transfer that can arise when a metal ion coordinates with O_2 : an end-on metal-superoxo adduct ($\eta^1 \text{ M-O}_2^-$) and a side-on metal-superoxo adduct ($\eta^2 \text{ M-O}_2^-$).^{59–61} These two adducts are primarily differentiated based on the distance and strength of the O–O bond. Both the metal center and ligand denticity significantly influence the formation of either an $\eta^1 \text{ M-O}_2^-$ or an $\eta^2 \text{ M-O}_2^-$ intermediate. Previous studies employing Raman spectroscopy and DFT calculations have revealed that the O_2 binding mode of a mononuclear Cu(II)- O_2^- complex can vary depending on the ligand denticity.^{57,61} Specifically, tridentate Cu(II) complexes predominantly favour the side-on O_2 binding mode, while tetradentate Cu(II) complexes promote the end-on O_2 binding mode. On the other hand, owing to the coordination behaviours of Ni(II) and Mn(III) centers, it is likely that tridentate Ni(II) complexes and tridentate Mn(III) complexes support the end-on O_2 binding mode.^{58,59} However, these intermediates have not been isolated in a HBM setting and characterized during the ORR due to their short lifetimes. Therefore, considering the observed differences in ORR selectivity among M-TPY SAMs, we proposed that $\eta^2 \text{ Cu-O}_2^-$ intermediates are generated in Cu-TPY SAM during the ORR, while $\eta^1 \text{ Ni-O}_2^-$ and $\eta^1 \text{ Mn-O}_2^-$ intermediates are formed in Ni-TPY SAM and Mn-TPY SAM, respectively. Due to the longer O–O bond length ($\sim 1.4\text{--}1.5 \text{ \AA}$) in side-on superoxide than in end-on superoxide ($\sim 1.2\text{--}1.3 \text{ \AA}$), breaking the longer and weaker O–O bond in side-on superoxide requires less energy and is therefore more kinetically facile than breaking the shorter and stronger O–O bond in end-on superoxide.^{59–61} Consequently, considering the formation of distinct M–O intermediates and the associated facilitation of O–O bond cleavage, we postulated that the 4-electron ORR selectivity observed in Cu-TPY SAM is likely attributed to the generation of $\eta^2 \text{ Cu-O}_2^-$ intermediates which facilitate the dissociative 4-electron ORR mechanism through efficient O–O

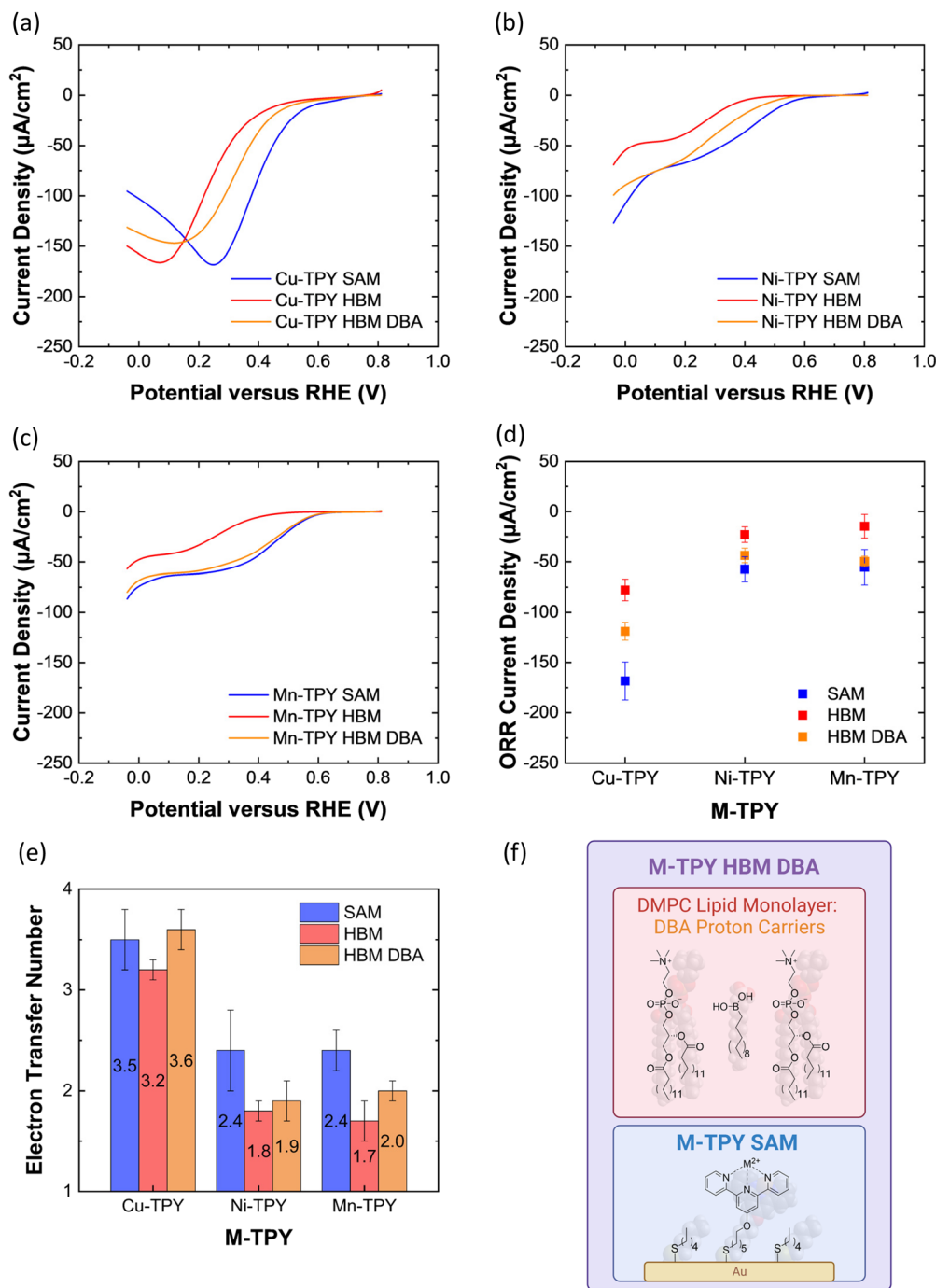


Fig. 5 Oxygen reduction activity (a–d) and selectivity (e) of M-TPY HBM (M = Cu, Ni, Mn). (a–c) Linear sweep voltammograms of a SAM of M-TPY (blue) covered by a monolayer of DMPC lipids (red) or a monolayer of DMPC lipids incorporated with 1 molar equivalent of DBA (orange) in an O₂-saturated 100 mM pH 7 sodium phosphate buffer solution at a scan rate of 10 mV s⁻¹. (d) ORR current densities measured at 0.252 V (versus RHE) for Cu-TPY HBM, 0.282 V (versus RHE) for Ni-TPY HBM, and 0.317 V (versus RHE) for Mn-TPY HBM. (f) Schematics of M-TPY HBM DBA.

bond cleavage (Fig. 6). The high ORR activity and H₂O selectivity of Cu-TPY SAM are reminiscent of the excellent catalytic performance of natural copper enzymes, such as laccase, ascorbate oxidase, and ceruloplasmin, which are well-known for exhibiting the 4-electron reduction of O₂ to water.^{62–64} On

the other hand, the 2-electron ORR selectivity observed in Ni-TPY SAM and Mn-TPY SAM can be attributed to the formation of η^1 Ni–O₂⁻ and η^1 Mn–O₂⁻ intermediates which proceed *via* the associative 2-electron ORR mechanism involving more hindered O–O bond cleavage.

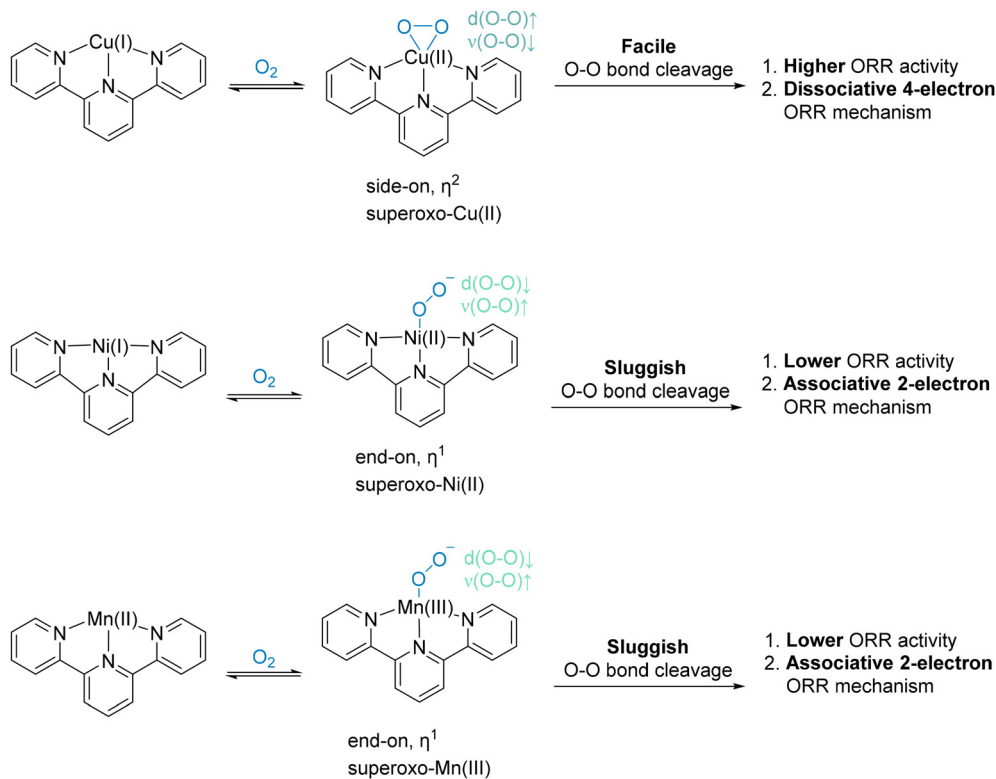


Fig. 6 Formation of distinct M–O intermediates in M-TPY SAMs (M = Cu, Ni, Mn) upon O₂ binding to the metal center leads to variations in their ORR activity and selectivity.

3.4. Mechanistic understanding of how the lipid nanoenvironment steers both the ORR kinetics and mechanism

Throughout the analysis of the ORR activity of M-TPY HBM, we observed a consistent pattern in the changes of ORR kinetics for Cu-TPY HBM, Ni-TPY HBM, and Mn-TPY HBM across different protonic nanoenvironments. By transitioning from a facile H⁺ transfer state (M-TPY SAM) to a H⁺ excluded state (M-TPY HBM), and ultimately to a H⁺ transfer regulated state (M-TPY HBM PC), similar patterns emerged (Fig. 5a–d). In the case of Cu-TPY SAM, in which unrestricted proton diffusion occurs in the bulk electrolyte, the ORR current density reached $168.4 \pm 18.9 \mu\text{A cm}^{-2}$ at a peak potential of $0.252 \pm 0.012 \text{ V}$ (*versus* RHE) (Fig. 5a and d). However, with the appendage of a DMPC lipid monolayer to form Cu-TPY HBM, there was a 53.8% decrease in current density to $77.8 \pm 17.7 \mu\text{A cm}^{-2}$ at 0.252 V (*versus* RHE). This decrease suggests that the hydrophobic lipid monolayer hampers the ORR kinetics by impeding transmembrane proton delivery. Due to limited proton availability, O₂ is reduced to superoxide, leading to a non-zero ORR current density. Subsequently, upon introducing 1 molar equivalent of DBA into the lipid monolayer of Cu-TPY HBM, a significant recovery of 70.7% in the ORR current density was observed compared to Cu-TPY SAM. This recovery resulted in a measured current density of $118.9 \pm 23.8 \mu\text{A cm}^{-2}$ at 0.252 V (*versus* RHE). The presence of DBA likely established an augmented pathway for proton transport through the lipid mono-

layer, facilitating a greater influx of protons to reach the Cu-TPY SAM surface and actively participate in the ORR. This enhanced proton flux, in turn, led to a higher current density. Thus, the recovery of the ORR current density in Cu-TPY HBM DBA highlights the significance of integrating proton carriers to modify the ORR kinetics. Similar trends were observed when adding a DMPC lipid monolayer and incorporating 1 molar equivalent of DBA for Ni-TPY SAM and Mn-TPY SAM. For Ni-TPY SAM, the inclusion of a DMPC lipid monolayer resulted in a 60.0% decrease in the ORR current density at a peak potential of $0.282 \pm 0.027 \text{ V}$ (*versus* RHE) (Fig. 5b and d). However, the subsequent incorporation of 1 molar equivalent of DBA led to a recovery of the ORR current density by 76.2%. Likewise, for Mn-TPY SAM, the addition of a DMPC lipid monolayer caused a 73.6% decrease in the ORR current density at $0.317 \pm 0.019 \text{ V}$ (*versus* RHE), while the introduction of 1 molar equivalent of DBA resulted in a substantial recovery of 89.7% in the ORR current density (Fig. 5c and d).

Apart from employing a DMPC lipid monolayer alone in the formation of M-TPY HBM, we further investigated the influence of incorporating cholesterol into the lipid monolayer on the protonic nanoenvironment encountered by M-TPY SAM and its subsequent impacts on the ORR kinetics. Previous studies examining the role of cholesterol in membrane fusion have demonstrated its ability to decrease fluidity, increase thickness, and enhance the compressibility of the lipid membrane.^{65–67} As a result, we hypothesized that the altered

mechanical properties of the lipid monolayer in M-TPY HBM obstructs proton permeation through the lipid monolayer. Moreover, cholesterol has the capability to occupy membrane defects, further limiting the availability of defects for transmembrane proton transfer, thus leading to lower ORR kinetics. By incorporating 20% w/w cholesterol into the DMPC lipid monolayer on M-TPY SAM, we compared the ORR current density of M-TPY HBM with and without cholesterol. Our experimental findings indicated that M-TPY HBM with cholesterol exhibited significantly lower ORR current density than M-TPY HBM alone (Fig. S10 and S12[†]). This observation suggests that the presence of cholesterol further impedes the transmembrane proton transfer kinetics, consequently lowering the ORR kinetics. Furthermore, we extended our investigation to evaluate whether incorporating proton carriers could restore the kinetics of transmembrane proton transfer in the cholesterol-infiltrated lipid layer. However, the results revealed that the inclusion of DBA did not contribute to ORR activity recovery (Fig. S11 and S12[†]). This lack of effect can be associated with the rigidity of the lipid monolayer caused by cholesterol, impairing the flip-flop motion of proton carriers, and hindering their effective delivery of protons across the lipid membrane.

On the other hand, regarding the ORR selectivity of M-TPY HBM, upon introducing a DMPC lipid monolayer into M-TPY SAM, a significant decrease in the number of electrons transferred per O₂ was observed. Specifically, Cu-TPY HBM exhibited a decrease from 3.5 ± 0.3 to 3.2 ± 0.1, while Ni-TPY HBM and Mn-TPY HBM experienced a decrease from 2.4 ± 0.4 to 1.8 ± 0.1 and from 2.4 ± 0.2 to 1.7 ± 0.2, respectively (Fig. 5e). The discrepancies in ORR selectivity between M-TPY SAM and M-TPY HBM can be ascribed to the hydrophobic properties of the lipid monolayer which hinders the proton transfer kinetics. Consequently, in M-TPY HBM, the rate of proton transfer from the bulk electrolyte to the M-TPY SAM surface becomes significantly slower than in no lipid case. Under conditions where proton transfer is notably slow and potentially absent, O₂ tends to undergo 1-electron reduction, resulting in the prevalence of a 1-electron ORR mechanism. Experimental evidence indicated that the ORR in M-TPY HBM occurred through a combination of 1-electron and 4-electron transfer pathways in the case of Cu-TPY HBM or a mixture of 1-electron and 2-electron transfer pathways in the cases of Ni-TPY HBM and Mn-TPY HBM. By incorporating 1 molar equivalent of DBA in M-TPY HBM, the 4-electron ORR selectivity in Cu-TPY HBM DBA and the 2-electron ORR selectivity in Ni-TPY HBM DBA and Mn-TPY HBM DBA were restored. This restoration occurred by recovering the kinetics of transmembrane proton transfer. Specifically, the number of electrons transferred was restored from 3.2 ± 0.1 to 3.6 ± 0.2 in Cu-TPY HBM DBA, from 1.8 ± 0.1 to 1.9 ± 0.2 in Ni-TPY HBM DBA, and from 1.7 ± 0.2 to 2.0 ± 0.1 in Mn-TPY HBM DBA (Fig. 5e). This observation can be attributed to the alleviation of proton transfer inhibition caused by the hydrophobic nature of the lipid monolayer, as the presence of proton carriers in the lipid monolayer restores the transmembrane delivery of protons from the bulk

electrolyte to the M-TPY SAM surfaces. Drawing from the empirical findings, we concluded that the ORR selectivity of M-TPY SAM is highly dependent on the formation of M–O intermediates, while the ORR selectivity of M-TPY HBM, in turn, depends on the proton availability and transfer rate.

4. Conclusions

This work has examined how proton transfer kinetics influences the ORR activity and selectivity of Cu-TPY, Ni-TPY, and Mn-TPY electrocatalysts installed at the SAM terminus. Upon the strategic integration of a DMPC lipid monolayer embedded with DBA proton carriers, the protonic nanoenvironment of M-TPY SAM, M-TPY HBM, and M-TPY HBM DBA was systematically explored. The presence of both the lipid monolayer and the proton carriers had synergistic effects on their ORR activity and selectivity. Specifically, the appendage of a DMPC lipid monolayer onto M-TPY SAM, forming M-TPY HBM, led to deceleration of the proton transfer kinetics due to the hydrophobic nature of the lipid membrane that prevents the passage of protons towards the ORR active sites. This phenomenon consequently imposed limitations on the ORR kinetics, which is a PCET reaction that requires efficient proton transfer. Interestingly, the introduction of DBA proton carriers into M-TPY HBM, forming M-TPY HBM DBA, effectively restored the ORR kinetics by expediting the transmembrane proton delivery across the lipid monolayer. This observation underscores the strong interdependence of the ORR behaviour of M-TPY SAM on the protonic nanoenvironment. Given the importance of both proton availability and transfer kinetics in influencing ORR activity and selectivity, this work establishes a strong foundation for investigating other PCET reactions in which tuning the electrochemical activity and selectivity holds the key to enhancing catalytic efficiency or yielding higher quantities of valuable chemicals. Additionally, we observed distinct variations in the ORR activity and selectivity among M-TPY SAMs. These differences were attributed to the formation of unique M–O intermediates upon O₂ binding to the metal centers. The contrasting characteristics of O–O bonds between end-on superoxide and side-on superoxide led to variations in O–O bond cleavage kinetics, ultimately influencing the ORR activity and selectivity. We proposed that the higher ORR activity and the 4-electron ORR selectivity observed in Cu-TPY SAM are likely due to the generation of η^2 Cu–O₂[−] intermediates. These intermediates facilitate a dissociative 4-electron ORR mechanism through more kinetically facile O–O bond cleavage. In contrast, the lower ORR activity and the 2-electron ORR selectivity observed in Ni-TPY SAM and Mn-TPY SAM are associated with the formation of η^1 Ni–O₂[−] and η^1 Mn–O₂[−] intermediates which proceed *via* an associative 2-electron ORR mechanism involving more kinetically sluggish O–O bond cleavage. This tunable protonic nanoenvironment holds promise to optimize the PCET steps of redox processes that are instrumental in achieving carbon neutrality and green production.

Author contributions

H. T. Y. and E. C. M. T. designed the project. Z. H. Y. conducted ligand synthesis and characterization. H. T. Y. conducted SAM formation, HBM fabrication, electrochemical measurements, and electrode characterization such as ICP-MS. All authors contributed to data interpretation and discussion as well as manuscript drafting and revision.

Conflicts of interest

The authors declare no competing financial interest.

Acknowledgements

E. C. M. T. would like to express gratitude to the National Natural Science Foundation of China for providing a Young Scientists Fund (NSFC: 22002132) on an interfacial electrocatalysis project. H. T. Y. and Z. H. Y. were supported by the Shenzhen Science and Technology Innovation Commission Basic Science General Program (SZSTI: JCYJ20210324122011031) and the URC Postdoctoral Fellowship Scheme, respectively. The authors thank Prof. Heng-Liang Wu at the National Taiwan University for providing substrates as electrodes in this study. The authors also thank the Research Grants Council in Hong Kong for an EU–HK Research and Innovation Cooperation Co-funding Mechanism (RGC: E-HKU704/19), a Theme-based Research Scheme (TRS: T23-713/22-R), Research Matching Grant Schemes (RMGS: 207301212, 207301251), an Early Career Scheme (ECS: 27301120), and a General Research Fund (GRF: 17308323) for enhancing the nanomaterial preparation facility at the HKU-CAS Joint Laboratory on New Materials and supporting research activities on green electrocatalysis and clean energy conversion.

References

- 1 S. Chu and A. Majumdar, *Nature*, 2012, **488**, 294–303.
- 2 L. Winkler, D. Pearce, J. Nelson and O. Babacan, *Nat. Commun.*, 2023, **14**, 2357.
- 3 P. P. Edwards, V. L. Kuznetsov, W. I. F. David and N. P. Brandon, *Energy Policy*, 2008, **36**, 4356–4362.
- 4 A. M. Oliveira, R. R. Beswick and Y. Yan, *Curr. Opin. Chem. Eng.*, 2021, **33**, 100701.
- 5 M. K. Singla, P. Nijhawan and A. S. Oberoi, *Environ. Sci. Pollut. Res.*, 2021, **28**, 15607–15626.
- 6 Y. Manoharan, S. E. Hosseini, B. Butler, H. Alzhahrani, B. T. Senior, T. Ashuri and J. Krohn, *Appl. Sci.*, 2019, **9**.
- 7 B. Pivovar, *Nat. Catal.*, 2019, **2**, 562–565.
- 8 O. Bethoux, *Energies*, 2020, **13**, 5843.
- 9 M. A. Aminudin, S. K. Kamarudin, B. H. Lim, E. H. Majilan, M. S. Masdar and N. Shaari, *Int. J. Hydrogen Energy*, 2023, **48**, 4371–4388.

- 10 C. Bergero, G. Gosnell, D. Gielen, S. Kang, M. Bazilian and S. J. Davis, *Nat. Sustain.*, 2023, **6**, 404–414.
- 11 K. Scott and A. K. Shukla, *Rev. Environ. Sci. Bio/Technol.*, 2004, **3**, 273–280.
- 12 W. Liu, H. Zhong, R. Wang and N. C. Seeman, *Angew. Chem., Int. Ed.*, 2011, **50**, 264–267.
- 13 M. K. Debe, *Nature*, 2012, **486**, 43–51.
- 14 N. Guerrero Moreno, M. Cisneros Molina, D. Gervasio and J. F. Pérez Robles, *Renewable Sustainable Energy Rev.*, 2015, **52**, 897–906.
- 15 G. Wang, Y. Yu, H. Liu, C. Gong, S. Wen, X. Wang and Z. Tu, *Fuel Process. Technol.*, 2018, **179**, 203–228.
- 16 S. P. Jiang and Q. Li, in *Introduction to Fuel Cells: Electrochemistry and Materials*, ed. S. P. Jiang and Q. Li, Springer Singapore, Singapore, 2022, pp. 173–228.
- 17 M. H. V. Huynh and T. J. Meyer, *Chem. Rev.*, 2007, **107**, 5004–5064.
- 18 C. Song and J. Zhang, in *PEM Fuel Cell Electrocatalysts and Catalyst Layers: Fundamentals and Applications*, ed. J. Zhang, Springer London, London, 2008, pp. 89–134.
- 19 D. R. Weinberg, C. J. Gagliardi, J. F. Hull, C. F. Murphy, C. A. Kent, B. C. Westlake, A. Paul, D. H. Ess, D. G. McCafferty and T. J. Meyer, *Chem. Rev.*, 2012, **112**, 4016–4093.
- 20 M. T. M. Koper, *Chem. Sci.*, 2013, **4**, 2710–2723.
- 21 V. Tripković, E. Skúlason, S. Siahrostami, J. K. Nørskov and J. Rossmeisl, *Electrochim. Acta*, 2010, **55**, 7975–7981.
- 22 M. T. M. Koper, *J. Electroanal. Chem.*, 2011, **660**, 254–260.
- 23 H. S. Casalongue, S. Kaya, V. Viswanathan, D. J. Miller, D. Friebel, H. A. Hansen, J. K. Nørskov, A. Nilsson and H. Ogasawara, *Nat. Commun.*, 2013, **4**, 2817.
- 24 J.-C. Dong, X.-G. Zhang, V. Briega-Martos, X. Jin, J. Yang, S. Chen, Z.-L. Yang, D.-Y. Wu, J. M. Feliu, C. T. Williams, Z.-Q. Tian and J.-F. Li, *Nat. Energy*, 2019, **4**, 60–67.
- 25 S. Wang, E. Zhu, Y. Huang and H. Heinz, *Sci. Adv.*, 2021, **7**, eabb1435.
- 26 M. Luo and M. T. M. Koper, *Nat. Catal.*, 2022, **5**, 615–623.
- 27 Y. Yang, R. G. Agarwal, P. Hutchison, R. Rizo, A. V. Soudackov, X. Lu, E. Herrero, J. M. Feliu, S. Hammes-Schiffer, J. M. Mayer and H. D. Abruña, *Nat. Chem.*, 2023, **15**, 271–277.
- 28 C. J. Barile, E. C. M. Tse, Y. Li, T. B. Sobyra, S. C. Zimmerman, A. Hosseini and A. A. Gewirth, *Nat. Mater.*, 2014, **13**, 619–623.
- 29 E. C. M. Tse, C. J. Barile, N. A. Kirchschrager, Y. Li, J. P. Gewargis, S. C. Zimmerman, A. Hosseini and A. A. Gewirth, *Nat. Mater.*, 2016, **15**, 754–759.
- 30 P. Lang, N. Yuan, Q. Jiang, Y. Zhang and J. Tang, *Energy Technol.*, 2020, **8**, 1900984.
- 31 P. K. Shen, *Electrochemical Oxygen Reduction: Fundamental and Applications*, Springer, Singapore, 1st 2021 edn, 2021.
- 32 M. Shao, Q. Chang, J.-P. Dodelet and R. Chenitz, *Chem. Rev.*, 2016, **116**, 3594–3657.
- 33 J. Liu, M. Jiao, L. Lu, H. M. Barkholtz, Y. Li, Y. Wang, L. Jiang, Z. Wu, D.-j. Liu, L. Zhuang, C. Ma, J. Zeng,

- 1 B. Zhang, D. Su, P. Song, W. Xing, W. Xu, Y. Wang, Z. Jiang and G. Sun, *Nat. Commun.*, 2017, **8**, 15938.
- 34 D. Banham, J. Zou, S. Mukerjee, Z. Liu, D. Yang, Y. Zhang, Y. Peng and A. Dong, *J. Power Sources*, 2021, **490**, 229515.
- 5 35 J. Zhao, C. Fu, K. Ye, Z. Liang, F. Jiang, S. Shen, X. Zhao, L. Ma, Z. Shadike, X. Wang, J. Zhang and K. Jiang, *Nat. Commun.*, 2022, **13**, 685.
- 36 J. H. Bae, R. F. Brocenschi, K. Kisslinger, H. L. Xin and M. V. Mirkin, *Anal. Chem.*, 2017, **89**, 12618–12621.
- 10 37 F. Jaouen, E. Proietti, M. Lefèvre, R. Chenitz, J.-P. Dodelet, G. Wu, H. T. Chung, C. M. Johnston and P. Zelenay, *Energy Environ. Sci.*, 2011, **4**, 114–130.
- 38 M. Kiani, X. Q. Tian and W. Zhang, *Coord. Chem. Rev.*, 2021, **441**, 213954.
- 15 39 J. Liu, C. Lee, Y. Hu, Z. Liang, R. Ji, X. Y. D. Soo, Q. Zhu and Q. Yan, *SmartMat*, 2023, **4**, e1210.
- 40 P. Rao, D. Wu, T.-J. Wang, J. Li, P. Deng, Q. Chen, Y. Shen, Y. Chen and X. Tian, *eScience*, 2022, **2**, 399–404.
- 20 41 H. Yang, Y. Liu, X. Liu, X. Wang, H. Tian, G. I. N. Waterhouse, P. E. Kruger, S. G. Telfer and S. Ma, *eScience*, 2022, **2**, 227–234.
- 42 H. Jia, Z. Sun, D. Jiang, S. Yang and P. Du, *Inorg. Chem. Front.*, 2016, **3**, 821–827.
- 25 43 M. K. Kadirov, S. T. Minzanova, I. R. Nizameev, L. G. Mironova, I. F. Gilmudinov, M. N. Khrizanforov, K. V. Kholin, A. R. Khamatgalimov, V. A. Semyonov, V. I. Morozov, D. M. Kadirov, A. R. Mukhametzyanov, Y. H. Budnikova and O. G. Sinyashin, *Inorg. Chem. Front.*, 2018, **5**, 780–784.
- 30 44 Y. Wang, Y. Yang, S. Jia, X. Wang, K. Lyu, Y. Peng, H. Zheng, X. Wei, H. Ren, L. Xiao, J. Wang, D. A. Muller, H. D. Abreuña, B. J. Hwang, J. Lu and L. Zhuang, *Nat. Commun.*, 2019, **10**, 1506.
- 35 45 K. Chen, K. Liu, P. An, H. Li, Y. Lin, J. Hu, C. Jia, J. Fu, H. Li, H. Liu, Z. Lin, W. Li, J. Li, Y.-R. Lu, T.-S. Chan, N. Zhang and M. Liu, *Nat. Commun.*, 2020, **11**, 4173.
- 40 46 R. P. Gautam, Y. T. Lee, G. L. Herman, C. M. Moreno, E. C. M. Tse and C. J. Barile, *Angew. Chem., Int. Ed.*, 2018, **57**, 13480–13483.
- 47 T. Zeng, R. P. Gautam, C. J. Barile, Y. Li and E. C. M. Tse, *ACS Catal.*, 2020, **10**, 13149–13155.
- 48 T. Zeng, R. P. Gautam, D. H. Ko, H.-L. Wu, A. Hosseini, Y. Li, C. J. Barile and E. C. M. Tse, *Nat. Rev. Chem.*, 2022, **6**, 862–880.
- 49 A. Hosseini, C. J. Barile, A. Devadoss, T. A. Eberspacher, R. A. Decreau and J. P. Collman, *J. Am. Chem. Soc.*, 2011, **133**, 11100–11102.
- 50 C. J. Barile, E. C. M. Tse, Y. Li, J. P. Gewargis, N. A. Kirchschrager, S. C. Zimmerman and A. A. Gewirth, *Biophys. J.*, 2016, **110**, 2451–2462.
- 51 T. Zeng, H.-L. Wu, Y. Li, E. C. M. Tse and C. J. Barile, *Electrochim. Acta*, 2019, **320**, 134611.
- 52 E. M. Miner, T. Fukushima, D. Sheberla, L. Sun, Y. Surendranath and M. Dincă, *Nat. Commun.*, 2016, **7**, 10942.
- 53 J. Park, Z. Chen, R. A. Flores, G. Wallnerström, A. Kulkarni, J. K. Nørskov, T. F. Jaramillo and Z. Bao, *ACS Appl. Mater. Interfaces*, 2020, **12**, 39074–39081.
- 15 54 J. Li, M. Chen, D. A. Cullen, S. Hwang, M. Wang, B. Li, K. Liu, S. Karakalos, M. Lucero, H. Zhang, C. Lei, H. Xu, G. E. Sterbinsky, Z. Feng, D. Su, K. L. More, G. Wang, Z. Wang and G. Wu, *Nat. Catal.*, 2018, **1**, 935–945.
- 20 55 H. Tian, L. Zeng, Y. Huang, Z. Ma, G. Meng, L. Peng, C. Chen, X. Cui and J. Shi, *Nano-Micro Lett.*, 2020, **12**, 161.
- 56 M. Magini, *Inorg. Chem.*, 1982, **21**, 1535–1538.
- 57 R. Cao, C. Saracini, J. W. Ginsbach, M. T. Kieber-Emmons, M. A. Siegler, E. I. Solomon, S. Fukuzumi and K. D. Karlin, *J. Am. Chem. Soc.*, 2016, **138**, 7055–7066.
- 25 58 A. T. Fiedler and A. A. Fischer, *JBIC, J. Biol. Inorg. Chem.*, 2017, **22**, 407–424.
- 59 G. M. Yee and W. B. Tolman, *Met. Ions Life Sci.*, 2015, **15**, 131–204.
- 60 P. L. Holland, *Dalton Trans.*, 2010, **39**, 5415–5425.
- 30 61 K. D. Karlin, W. B. Tolman, S. Kaderli and A. D. Zuberbühler, *J. Mol. Catal. A: Chem.*, 1997, **117**, 215–222.
- 62 H. Schweiger, E. Vayner and A. B. Anderson, *Electrochem. Solid-State Lett.*, 2005, **8**, A585.
- 35 63 D. J. Kosman, *JBIC, J. Biol. Inorg. Chem.*, 2010, **15**, 15–28.
- 64 M. S. Thorum, C. A. Anderson, J. J. Hatch, A. S. Campbell, N. M. Marshall, S. C. Zimmerman, Y. Lu and A. A. Gewirth, *J. Phys. Chem. Lett.*, 2010, **1**, 2251–2254.
- 40 65 H. Ohvo-Rekilä, B. Ramstedt, P. Leppimäki and J. Peter Slotte, *Prog. Lipid Res.*, 2002, **41**, 66–97.
- 66 S.-T. Yang, A. J. B. Kreutzberger, J. Lee, V. Kiessling and L. K. Tamm, *Chem. Phys. Lipids*, 2016, **199**, 136–143.
- 45 67 W. K. Subczynski, M. Pasenkiewicz-Gierula, J. Widomska, L. Mainali and M. Raguz, *Cell Biochem. Biophys.*, 2017, **75**, 369–385.